

Probing The Dark Matter Halo of High-redshift Quasar from Wide-Field Clustering Analysis

HAO MENG (蒙皓),¹ HUANIAN ZHANG (张华年),^{1,2} AND GUANGPING YE (叶广平)¹¹*Department of Astronomy, Huazhong University of Science and Technology, Wuhan, Hubei 430074, China*²*Steward Observatory, University of Arizona, Tucson, AZ 85719, USA*

ABSTRACT

High-redshift quasars have been an excellent tracer to study the astrophysics and cosmology at early Universe. Using 216,949 high-redshift quasar candidates ($5.0 \leq z < 6.3$) selected via machine learning from the Legacy Survey Data Release 9 and the Wide-field Infrared Survey Explorer, we perform wide-field clustering analysis to investigate the large-scale environment of those high-redshift quasars. We construct the projected auto correlation function of those high-redshift quasars that is weighted by its predicted probability of being a true high-redshift quasar, from which we derive the bias parameter and the typical dark matter halo mass of those quasars. The dark matter halo mass of quasars estimated from the projected auto correlation function is $\log(M_h/M_\odot) = 12.2^{+0.2}_{-0.7}$ ($11.9^{+0.3}_{-0.7}$), with the bias parameter b of $12.34^{+4.26}_{-4.37}$ ($11.52^{+4.02}_{-4.14}$) for the redshift interval of $5.0 \leq z < 5.7$ ($5.7 \leq z < 6.3$). Our results, combined with other measurements of dark matter halo masses for quasars or active galactic nucleus which obtain a lower dark matter halo mass of $\sim 10^{11.5} M_\odot$ at similar redshift, suggest a more complex, and possibly non-monotonic evolution of quasar hosting dark matter halo. Moreover, we estimate the duty cycle of those quasars, which is $0.008^{+0.135}_{-0.007}$ ($0.003^{+0.047}_{-0.003}$) for the redshift interval of $5.0 \leq z < 5.7$ ($5.7 \leq z < 6.3$).

Keywords: cosmology: observations – quasars: high-redshift – quasars: search

1. INTRODUCTION

Quasars are exceptionally luminous objects that can be observed even at very early Universe, with a few observed at $z > 7.5$ (Bañados et al. 2018; Yang et al. 2020; Wang et al. 2021). They are powered by gas accretion onto a supermassive black hole (SMBH) residing at the center of a galaxy, which is embedded within a dark matter halo (DMH). These SMBHs accrete gas from its surrounding environment, and those activities may trigger intermittent but violent outbursts, resulting in significant feedback effect that could regulate the growth of both the SMBH and the central galaxy (Liu et al. 2025) and can ultimately affect the growth of the dark matter halo (Salpeter 1964; Lynden-Bell 1969; Kormendy & Richstone 1995).

The immediate environments of luminous high-redshift quasars are critically important for understanding the SMBH formation and its accretion. These environments may provide the exotic conditions necessary

for forming massive black hole seeds (e.g., Begelman et al. 2006; Regan et al. 2014; Inayoshi et al. 2020) and/or act as reservoirs for rapid, sustained gas accretion to fuel early growth (e.g., Di Matteo et al. 2005). To build a comprehensive model of early SMBH evolution – encompassing their rapid growth, their connection to large-scale structure, and their co-evolution with host galaxies – it is essential to observationally constrain the large-scale environments (e.g., Fan et al. 2006; Overzier et al. 2009; Drake et al. 2019) and the host dark matter halos of these quasars within the framework of cosmological structure formation (e.g., Zhang et al. 2023).

Statistically, the clustering analysis of quasars, commonly through the two-point auto correlation function (Peebles 1980), has proven to be a powerful tool to connect the large-scale properties of quasars with their hosting dark matter halos (Shanks & Boyle 1994; Croom et al. 2001). A key question about quasars and its corresponding large-scale environment is whether the most luminous quasars at high redshift, which trace the peaks of the density field, inhabit the same most massive dark matter halo that will evolve into the cores of present-day rich clusters, or they represent transient, merger-driven

phases in a moderate-mass systems. Therefore, studying the quasar's auto correlation function, inferring its DMH mass (M_h), as well as its evolution, offers a direct observational link to the life cycle of quasars and the assembly history of the massive DMH that serves as their foundational scaffolds. This approach bridges the gap between the small-scale physics of black hole accretion and the large-scale dynamics of structure formation in the Universe.

Moreover, to observationally constrain the growth scenarios of early SMBHs, two key quantities are essential: (1) the BH masses during active phases, and (2) the fraction of their total growth that occurs during the UV-bright, luminous quasar phase we observe. The quasar clustering analysis provides a direct observational handle on this second quantity via the duty cycle, f_{duty} . This is defined as the ratio of the observed quasar number density to the number density of their host dark matter halos: $f_{\text{duty}} \equiv \frac{n_{\text{quasar}}}{n_{\text{halo}}} \sim \frac{t_Q}{t_H}$, where t_Q is the typical quasar lifetime and t_H is the Hubble time at the redshift of observation (Efstathiou & Rees 1988; Cole & Kaiser 1989; Haiman & Hui 2001; Martini & Weinberg 2001). Under the standard assumption that each halo hosts a single luminous quasar phase of duration t_Q , f_{duty} represents the fraction of cosmic time that a typical halo shines as a quasar. A low duty cycle implies that most SMBH mass assembly must occur via radiatively inefficient or heavily obscured accretion, which contributes minimally to the observed UV luminosity.

At low-redshift epoch, the clustering analysis reveals that quasars are not randomly distributed but are preferentially located in regions of enhanced matter density (Croom et al. 2005; Shen et al. 2007; Ross et al. 2009; Krumpe et al. 2010; Shen et al. 2013; Ikeda et al. 2025). They are found to be biased tracers of the underlying cosmic web, inhabiting the knots and filaments where dark matter collapses to form massive halos. The bias parameter, b , and the scale length, r_0 , derived from the clustering analysis, are pivotal quantities, as they quantify the spatial concentration of quasars, and directly connect to the mass of the dark matter halo where those quasars reside. For example, Giner Mascarell et al. (2025) find that the scale length, r_0 , increases rapidly from $z = 0$ to $z = 4$ using a sample of ~ 1.3 million quasar candidates with magnitudes $G \leq 20.5$ from the Gaia-unWISE Quasar Catalog (Quaia). Research on the bias parameter and DMH mass across cosmological times can provide a basic insight into the coevolution of quasars and the large-scale environment they reside (e.g., Volonteri 2012). Therefore, the direct probe of the bias parameter and DMH mass at early Universe

is critical for us to fully understand the formation and evolution of SMBH and its host galaxies/halos.

Nowadays, there are more and more studies on the clustering analysis of quasars and the mass of dark matter halos at high redshift ($z > 5$) since the launch of James Webb Space Telescope (JWST, Gardner et al. 2023). For example, Arita et al. (2023) employs the quasar auto correlation function at $z \sim 6$, finding $M_h = 5.0_{-4.0}^{+7.4} \times 10^{12} h^{-1} M_\odot$ and a large bias $b = 20.8 \pm 8.7$. A subsequent analysis using active galactic nuclei (AGN)-galaxy cross-correlation (Arita et al. 2025) refines this to $\log_{10}(M_h/h^{-1} M_\odot) = 11.53_{-0.20}^{+0.15}$ for low-luminosity AGNs. At slightly lower redshifts, Lin et al. (2025) reports $\log_{10}(M_h/M_\odot) = 11.21_{-0.32}^{+0.35}$ for low-luminosity AGNs at $3.9 < z < 5.0$ and $\log_{10}(M_h/M_\odot) = 11.04_{-0.32}^{+0.34}$ for the $5.0 < z < 6.0$ bin. For more luminous quasars at $z \sim 6.25$, Eilers et al. (2024) infers a higher minimum halo mass of $\log_{10}(M_{h,\text{min}}/M_\odot) = 12.43_{-0.15}^{+0.13}$ from the quasar-galaxy cross-correlation. JWST observations now enable similar estimates for the highest-redshift sources. For a little red dot (LRD) and two quasars at $z = 7.3$, Schindler et al. (2025a,b) find $\log_{10}(M_{h,\text{min}}/M_\odot) = 12.0_{-1.0}^{+0.8}$ and $\log_{10}(M_{h,\text{min}}/M_\odot) = 11.64_{-0.64}^{+0.56}$, respectively.

Those pioneering studies of high-redshift AGNs, quasars and LRDs have provided first glimpses into their host dark matter halo, yet these results remain scarce, widely scattered, and highly uncertain. The lack of consensus stems from two key limitations: the comparably small sample sizes and extremely small survey areas which are susceptible to cosmic variance (e.g., Driver & Robotham 2010; Robertson 2010; Ucci et al. 2021). Those limitations can significantly bias the estimates of the bias parameter, the clustering strength and the derived dark matter halo properties.

To address these challenges, we present a wide-field clustering analysis of a large sample of high-redshift quasar candidates in order to mitigate the above limitations. The high-redshift quasar samples are robustly identified using a machine learning methodology (Ye et al. 2024) by combining g, r, z photometry from the Legacy Survey Data Release 9 (Dey et al. 2019; Schlegel et al. 2021) and $W1, W2$ photometry from the Wide-field Infrared Survey Explorer (WISE) all-sky survey (Wright et al. 2010; Mainzer et al. 2011), which covers an area of $\approx 17,000 \text{ deg}^2$. The machine learning technique is demonstrated to be quite effective in similar studies to search exotic objects using the same dataset (e.g., Zhang et al. 2025). The unprecedented combination of a large celestial area and a large data sample can effectively mitigate the cosmic variance, providing more reliable insights into the cosmic environment of

high-redshift quasars, the properties of their host dark matter halos, and their co-evolution history.

The paper is organized as follows. In Section 2, we present the data sample of high-redshift quasar candidates and the random sample used in this study. In Section 3, we present the clustering analysis, obtain the projected correlation function. We also derive the dark matter halo mass and the bias parameter from the clustering analysis. In Section 4, we discuss the derived quasar dark matter halo mass, and the quasars’ duty cycle. We summarize and conclude in Section 5. During this work, we adopt the cosmological model with $H_0 = 67.32 \text{ km s}^{-1} \text{ Mpc}^{-1}$, $\Omega_0 = 0.3158$ and $w_0 = -1$ (Planck Collaboration et al. 2020). The dimensionless Hubble constant, h , is defined to be $h = H_0/100$.

2. DATA

2.1. High-redshift Quasar Candidates

Ye et al. (2024) presents a detailed random forest classification model to search high-redshift quasars, here we briefly sketch the model. Using the g, r, z photometric measurements extracted from the *Dark Energy Spectroscopic Instrument (DESI) Legacy Imaging Surveys DR9* (LS DR9, Dey et al. 2019) and the $W1, W2$ photometric measurements from *Wide-field Infrared Survey Explorer* (WISE, Wright et al. 2010; Mainzer et al. 2011), the authors build two parallel random forest (RF) models with excellent performance: the “mag model” and the “flux model”. The difference lies in: the “mag model” uses the $g, r, z, W1, W2$ magnitudes as inputs while the “flux model” uses the $g, r, z, W1, W2$ fluxes as inputs (see Section 3 of Ye et al. (2024) for details). The “mag model” has a slightly higher precision but slightly lower completeness than the “flux model”.

There are 272,424 (568,188) high-redshift quasar candidates for the “mag model” (“flux model”) in the entire LS DR9 footprint, and the catalog includes the predicted probabilities of being a true high-redshift quasar from the classification model and the photometric redshifts estimated by a regression model. There are 216,949 overlapping candidates that are simultaneously identified by the “mag model” and the “flux model”, which will be the quasar sample we use in the following discussions because we are prioritizing sample purity. To obtain a sample of more reliable high-redshift quasar candidates, the authors impose probability thresholds. The first probability threshold (p_{thre}) is set to assure that the precision of the known high-redshift quasars in the predicted results can reach 100%. The second probability threshold is the highest probability assigned to a non-quasar object but misclassified as a high- z quasar. For the “mag model” (“flux model”), the two proba-

bility thresholds are 40.82%, 82.49% (40.03%, 75.23%) respectively.

DESI Data Release 1 (DR1) (DESI Collaboration et al. 2025) has already collected enormous spectra for tens of millions of astronomical objects, consisting of 13.1 million galaxies, 4 million Milky Way stars, and 1.6 million quasars, which deepens our understanding of the Universe and provides a great opportunity to verify the performance of our random forest classification model Ye et al. (2024). From an initial photometric selection of all high-redshift quasar candidates of the “flux model”, we identified 3,157 objects with spectroscopic observations in DESI DR1. Among them, 1,429 are compact galaxies, 1,190 are Milky Way stars, and 538 are quasars. The detailed verification of the model is presented in Ye, Zhang et al. (2026). Notably, as the predicted probability increases, the success rate of the high-redshift quasar candidates rises significantly, where the success rate is defined as the fraction of confirmed high-redshift quasars among all DESI DR1 observations of our candidates. For example, the success rate is $\lesssim 30\%$ if the first probability threshold is applied, the success rate reaches $\gtrsim 60\%$ if the second probability threshold is applied, and the success rate reaches $\gtrsim 70\%$ if probability threshold of 0.9 is applied, which is much higher than the success rate of the quasar classification for $5 \leq z < 6.5$ by the DESI team.

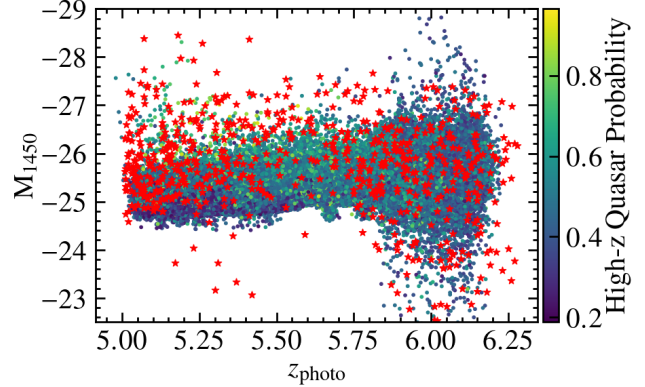


Figure 1. The distribution of M_{1450} versus photometric redshift for the 216,949 high-redshift quasar candidates, which are color-coded by its corresponding predicted probability. The red stars denote the true high-redshift quasars.

In Ye, Zhang et al. (2026), the authors also estimate the ultraviolet (UV) luminosity (expressed by the absolute magnitude at rest-frame 1450 Å) of those high-redshift quasars according to its photometric redshift, see details in Ye, Zhang et al. (2026). In Figure 1, we present the distribution of the absolute magnitude at rest-frame 1450 Å (M_{1450}) versus photometric red-

shift for these 216,949 candidates, with the known high-redshift quasars denoted by red stars, of which 130 are newly discovered high-redshift quasars in DESI DR1. The typical M_{1450} of those quasar candidates is ~ -25.5 at $z \lesssim 5.7$ and -25 at $5.7 \leq z < 6.3$. Obviously, the M_{1450} v.s. z distribution of the high-redshift quasar candidates is consistent with that of true high-redshift quasars, which demonstrates the reliability of our quasar candidates since they are not selected by M_{1450} .

We divide the entire quasar candidate sample into two redshift bins: a lower-redshift bin ($5.0 \leq z < 5.7$, median $z \sim 5.3$) and a higher-redshift bin ($5.7 \leq z < 6.3$, median $z \sim 6.0$). The sky distributions of candidates in these two redshift bins are shown in Figure 2. To optimize the trade-off between sample size and purity, we evaluate three probability thresholds (p_{thre}) to select the final quasar sample. As summarized in Table 1, these yield:

1. Low threshold ($p_{\text{thre}} = 0.41$): maximizes the sample size ($N = 66,343$ and $97,977$ for the two redshift bins, respectively) but with lower purity.
2. Intermediate threshold ($p_{\text{thre}} = 0.6$): balances sample size and purity ($N = 16,295$ and $21,590$ for the two redshift bins, respectively).
3. High threshold ($p_{\text{thre}} = 0.8$): maximizes the sample purity at the expense of sample size ($N = 2,429$ and $1,923$ for the two redshift bins, respectively).

Since the sample reliability is our primary concern, we adopt the most conservative threshold, $p_{\text{thre}} = 0.8$, for our baseline analysis. The implications of using less stringent thresholds are discussed in Section 4.1.

Table 1. The number of quasar candidates left after imposing each of the probability threshold p_{thre} .

p_{thre}	Number	
	$5.0 \leq z < 5.7$	$5.7 \leq z < 6.3$
0.41	66343	97977
0.6	16295	21590
0.8	2429	1923

2.2. Random Points Sample

The correctly constructed random quasar catalogs, which are truly uniformed distributed across the survey area and match the redshift distribution as the source catalog, are key to correctly constructing the auto correlation function of the quasars. We generate random quasar catalogs as follows. First, we sprinkle random

points across the entire celestial area with number density of $1/\text{arcmin}^2$, i.e. 148,510,660 points. Then, for each redshift group in the subsample corresponding to each p_{thre} , we select the corresponding random points. Random points within a circular neighborhood of radius $100 h^{-1} \text{ Mpc}$, which is large enough for the construction of correlation function, centered on the quasar sample will be selected. Next, the redshift of filtered random points is assigned to follow the redshift distribution of of each redshift group of quasar candidates. The comoving distances are derived from the corresponding redshifts based on the adopted cosmological model.

3. CLUSTERING ANALYSIS

We estimate the auto correlation function of high-redshift quasar candidates by measuring the projected correlation function $\omega_p(r_p)$ of quasar candidates in two redshift bins. We then estimate their uncertainties and derive the corresponding real space correlation function $\xi(r)$, which is assumed to be a power-law function characterized by the correlation length (r_0) and power-law index (γ). The details are the following.

3.1. Projected Correlation Function

To mitigate the effect of redshift-space distortions (RSD) on the measured clustering signal, we compute the two-dimensional correlation function $\xi(r_p, \pi)$, where r_p, π represents the decomposition of the three-dimensional distance between two objects (s): the separation perpendicular to the line of sight and parallel to the line of sight, respectively (i.e. $s = \sqrt{r_p^2 + \pi^2}$). There are various estimators to determine the projected correlation function and we adopt the estimation from Landy & Szalay (1993) as follows:

$$\xi(r_p, \pi) = \frac{DD(r_p, \pi) - 2DR(r_p, \pi) + RR(r_p, \pi)}{RR(r_p, \pi)} \quad (1)$$

where $DD(r_p, \pi)$, $DR(r_p, \pi)$, $RR(r_p, \pi)$ represent data-data, data-random, and random-random pair counts within each bin characterized by r_p and π , respectively. Because the primary high-redshift quasar sample we use are selected via photometry but not verified via spectroscopy, then it might not be a real quasar, thus we weight the pair counting by its corresponding predicted probability of being a true high-redshift quasar to obtain a more realistic estimation of the clustering signal.

We adopt `Corrfunc` (Sinha & Garrison 2020)¹, a Python package containing routines to perform the pair

¹ <https://github.com/manodeep/Corrfunc>

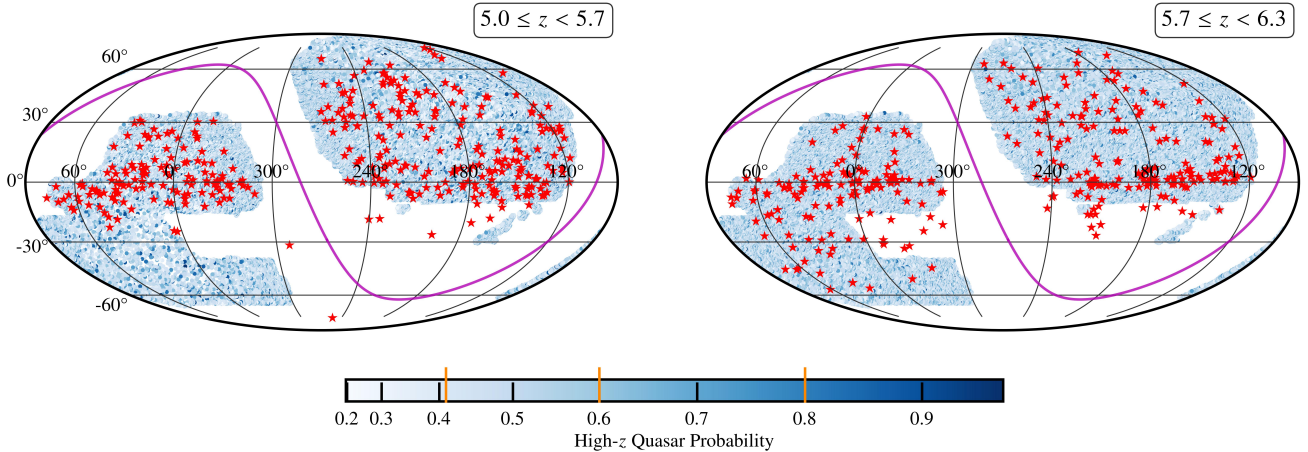


Figure 2. The sky distribution of quasar candidates for $5.0 \leq z < 5.7$ (left) and $5.7 \leq z < 6.3$ (right). The color coding denotes the predicted probability of being a high- z quasar obtained in Ye et al. (2024). Red stars represent the spectra-verified quasars within the same redshift range. Magenta solid line represent the Galactic plane. Orange solid lines in the color bar stand for the three probability thresholds of $p_{\text{thre}} = 0.41, 0.6, 0.8$.

counting for clustering analysis. The projected correlation function $\omega_p(r_p)$ is derived by integrating $\xi(r_p, \pi)$ within π direction.

$$\omega_p(r_p) = \int_{-\pi_{\max}}^{\pi_{\max}} \xi(r_p, \pi) d\pi = 2 \int_0^{\pi_{\max}} \xi(r_p, \pi) d\pi \quad (2)$$

where π_{\max} is the optimum limit above which the clustering signal is almost negligible. In this research, we adopt $\pi_{\max} = 90 h^{-1}\text{Mpc}$ that is consistent with the values in the literature.

There are different methods to estimate the statistical uncertainties of the auto correlation function measurement, either internally using bootstrap or jackknife resampling or externally using mock catalogs based on cosmological simulations. Here we adopt the jackknife resampling method (Zehavi et al. 2005) to estimate the uncertainty of the auto correlation function measurements $\omega_p(r_p)$. We divide the entire quasar candidates as well as the random points into $N = 20$ subsamples by roughly equal celestial area, and eliminate each of these subsamples in turn to measure the correlation function for the rest samples. The covariance error matrix is estimated as the following:

$$C_{ij} = \frac{N-1}{N} \sum_{k=1}^N (\omega_{p,k}(r_{p,i}) - \bar{\omega}_p(r_{p,i})) \times (\omega_{p,k}(r_{p,j}) - \bar{\omega}_p(r_{p,j})), \quad (3)$$

where $\omega_{p,k}(r_{p,i})$ and $\bar{\omega}_{p,k}(r_{p,i})$ represent the values of projected correlation function of the subsample in which the k th subsample is excluded within the i th r_p bin and the mean value of the projected correlation function of the same sample, respectively. The covariance matrix is generally dominated by the diagonal elements. The un-

certainty of $\omega_p(r_{p,i})$ is evaluated as the diagonal element of the covariance error matrix, $\sigma_i = C_{ii}$.

The projected correlation function is derived from the integration of the real-space correlation function $\xi(r)$ (Davis & Peebles 1983) as follows:

$$\omega_p(r_p) = 2 \int_{r_p}^{\infty} \frac{r \xi(r)}{\sqrt{r^2 - r_p^2}} dr, \quad (4)$$

where the real-space correlation function is normally assumed to follow a power-law function with a correlation length (r_0) and a power-law index (γ):

$$\xi(r) = \left(\frac{r}{r_0} \right)^{-\gamma}, \quad (5)$$

therefore the fitted correlation function $\omega_{p,\text{fit}}(r_p)$ is represented analytically as:

$$\frac{\omega_{p,\text{fit}}(r_p)}{r_p} = B \left(\frac{\gamma-1}{2}, \frac{1}{2} \right) \left(\frac{r_p}{r_0} \right)^{-\gamma}. \quad (6)$$

where B represents the beta function.

The quasar auto correlation function, $\omega_p(r_p)$, and its best fit are presented in Figure 3 for quasars at $5.0 \leq z < 5.7$ and $5.7 \leq z < 6.3$. Again we need to emphasize that we already weight the pair counting by its corresponding predicted probability of being a true high-redshift quasar in the calculation of the correlation function. The results using other probability thresholds are quite consistent with it, which will be discussed in detail in Sec. 4.1.

As can be seen that it is very challenging to probe the correlation at small scale ($r_p < \text{a few } h^{-1}\text{Mpc}$) due to the limitation of the data sample, since the faint quasars

can not be probed because of the observational sensitivity. The quasar auto correlation at a comparably large-scale radius shows excellent power-law behavior for both redshift intervals of $5.0 \leq z < 5.7$ and $5.7 \leq z < 6.3$, as shown in Figure 3. From the best-fitting to the observational correlation function, we obtain $r_0 = 20.76 \pm 6.18 h^{-1}\text{Mpc}$ and $\gamma = 1.17 \pm 0.05$ for quasars at $5.0 \leq z < 5.7$, while $r_0 = 15.09 \pm 8.62 h^{-1}\text{Mpc}$ and $\gamma = 1.30 \pm 0.15$ for quasars at $5.7 \leq z < 6.3$.

3.2. The Bias Parameter

Quasars, as one of the most luminous objects in the Universe, are assumed to reside in the densest part of dark matter distribution and trace the distribution of underlying dark matter (Sheth & Tormen 1999), with a certain bias. The bias parameter is defined to be the ratio of clustering strength between quasars and underlying dark matter at $r = 8h^{-1} \text{ Mpc}$;

$$b = \sqrt{\frac{\xi(8, z)}{\xi_{\text{DM}}(8, z)}} \quad (7)$$

where $\xi(8, z)$ is approximated by the power-law function defined by Eq.(5), and $\xi_{\text{DM}}(8, z)$ is usually estimated using `halomod` (Murray et al. 2013, 2021) package², assuming the bias model developed by Tinker et al. (2010), the transfer function from `CAMB`³, and the growth model proposed by Carroll (2000).

Based on the measured projected correlation function and the best-fit model, the bias parameters are estimated to be $12.34^{+4.26}_{-4.37}$ for $5.0 \leq z < 5.7$ and $11.52^{+4.02}_{-4.14}$ for $5.7 \leq z < 6.3$, respectively. The uncertainty of b is estimated by bootstrap uncertainty estimation using random sampling with replacement. We first generate a large amount of random samples of (r_0, γ) assuming they follow Gaussian distributions with the mean and standard deviation estimated above, and then we repeat the bootstrap resampling 1,000 times and calculate b as in Eq. (7). From the distribution of b measurements, we determine the mean value and we quote use the 16 and 84 percentiles as the uncertainty range. The results using other probability thresholds are consistent with those within 1 σ error bar and are listed in Table 2 for quasars at $5.0 \leq z < 5.7$ and $5.7 \leq z < 6.3$.

3.3. Dark Matter Halo Mass of the Quasars

We derive the typical dark matter halo mass from the bias parameters of the quasar auto correlation function. Under the standard assumption that quasars are biased

tracers of the underlying dark matter distribution, their effective bias $b(M_h, z)$ can be modeled via the halo occupation distribution (HOD) framework. Following Tinker et al. (2010), the large-scale bias of halos of mass M_h at redshift z is given by:

$$b(\nu) = 1 - A \frac{\nu^a}{\nu^a + \delta_c^a} + B\nu^b + C\nu^c, \quad (8)$$

where ν is the peak height of the linear density field and defined as $\nu = \delta_c/\sigma(R)$, δ_c is the critical density for the collapse of DMHs and $\sigma(R)$ is the linear matter variance on the Lagrangian scale of the halo, i.e., $R = (3M/4\pi\bar{\rho}_m)^{1/3}$. And $\sigma(R)$ is defined as

$$\sigma^2(R) = \frac{1}{2\pi^2} \int_0^{k_{\text{max}}} P(k, z) \hat{W}^2(k, R) k^2 dk, \quad (9)$$

where $P(k, z)$ is the matter power spectrum at redshift z and generated by `CAMB` with the adopted cosmological parameters, and R represents the radius of the DMH R_{halo} . \hat{W} is the Fourier transform of the top-hat window function of radius R . k_{max} is usually set to $10 h\text{Mpc}^{-1}$ in order for the above integration to converge. \hat{W} is defined as

$$\hat{W}(k, R) = \frac{3}{(kR)^3} [\sin(kR) - kR \cos(kR)]. \quad (10)$$

Solving Eq. (8) with the adopted parameters in Table 2 of Tinker et al. (2010), we can obtain R_{halo} , from which we can derive the typical mass of the DMH as

$$M_h = \frac{4}{3} \pi \bar{\rho}_m R_{\text{halo}}^3, \quad (11)$$

where $\bar{\rho}_m$ is the mean density of the Universe and is calculated to be $2.78 \times 10^{11} \Omega_m h^2 M_\odot/\text{Mpc}^3$ for both redshift bins.

According to the estimations of the bias parameter from the projected auto correlation function, the typical DMH masses of quasars are estimated to be $\log(M_h/M_\odot) = 12.2^{+0.2}_{-0.7}$ for $5.0 \leq z < 5.7$ and $\log(M_h/M_\odot) = 11.9^{+0.3}_{-0.7}$ for $5.7 \leq z < 6.3$. The uncertainty of $\log(M_h/M_\odot)$ are estimated by the bootstrap uncertainty method as well. The difference in the derived halo mass between the two subsamples is consistent with the difference in their median quasar luminosity, M_{1450} , suggesting a connection between AGN/quasar luminosity and the host halo mass. The large sky coverage and substantial co-moving volume of our data sample ensure that these estimates are robust against significant biases from cosmic variance. The DMH masses derived using other probability thresholds (see Table 2) are consistent with each other within their

² <https://github.com/halomod/halomod>

³ <https://github.com/cmbant/CAMB>

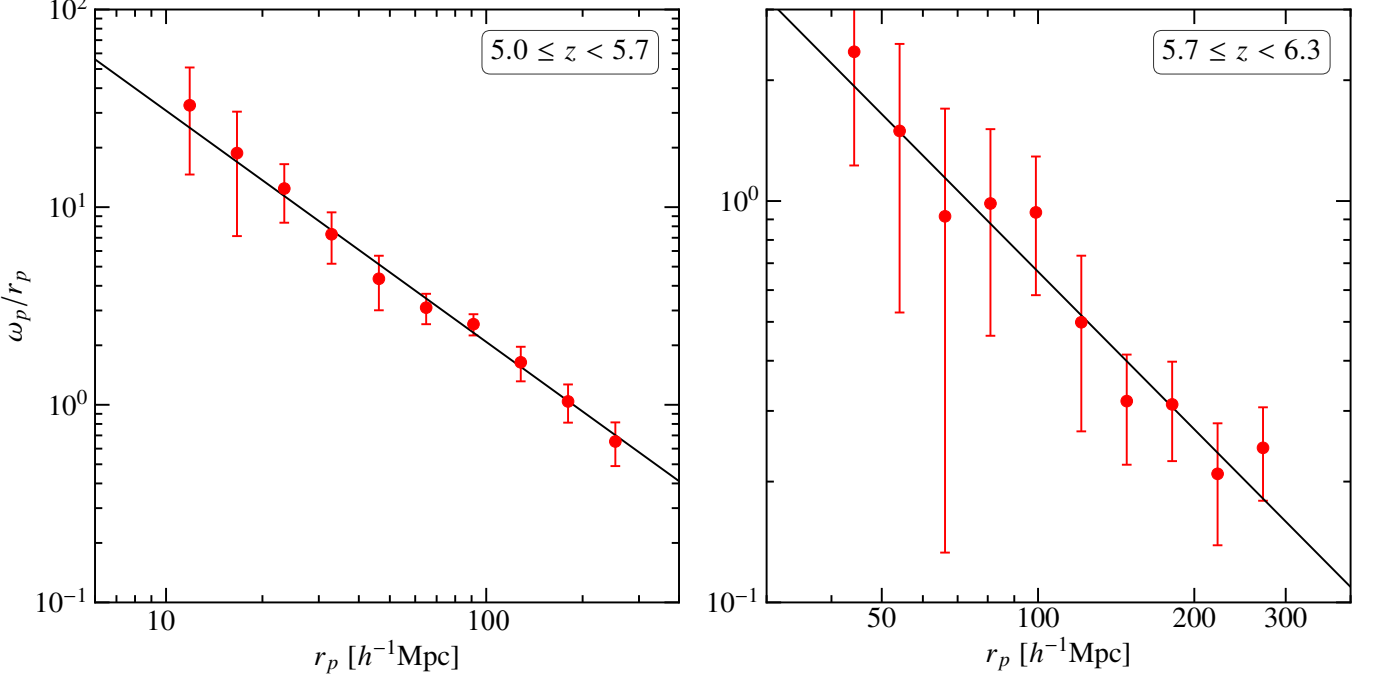


Figure 3. Projected auto correlation function for quasar at $5.0 \leq z < 5.7$ (left) and $5.7 \leq z < 6.3$ (right) with a probability threshold of $p_{\text{thre}} = 0.8$. The red dots represent the measurements of the projected auto correlation and the solid line stands for the best-fit model to the observational correlation.

errors. We note that the DMH mass estimation is sensitive to σ_8 , but the further discussions are out of the scope of this work.

5.0 ≤ z < 5.7				
p_{thre}	$r_0(h^{-1}\text{Mpc})$	γ	Bias	$\log(M_h/M_\odot)$
0.41	23.93 ± 1.37	1.16 ± 0.01	$13.14^{+0.44}_{-0.44}$	$12.2^{+0.1}_{-0.1}$
0.6	22.47 ± 2.16	1.16 ± 0.02	$12.66^{+0.71}_{-0.72}$	$12.2^{+0.1}_{-0.1}$
0.8	20.76 ± 6.18	1.17 ± 0.05	$12.34^{+4.26}_{-4.37}$	$12.2^{+0.2}_{-0.7}$
5.7 ≤ z < 6.3				
p_{thre}	$r_0(h^{-1}\text{Mpc})$	γ	Bias	$\log(M_h/M_\odot)$
0.41	7.49 ± 0.89	1.15 ± 0.02	$7.44^{+0.49}_{-0.49}$	$11.2^{+0.1}_{-0.1}$
0.6	7.21 ± 0.90	1.15 ± 0.02	$7.28^{+0.51}_{-0.51}$	$11.1^{+0.1}_{-0.1}$
0.8	15.09 ± 8.62	1.30 ± 0.15	$11.52^{+4.02}_{-4.14}$	$11.9^{+0.3}_{-0.7}$

Table 2. The best-fit results of our clustering analysis, as well as the derived halo properties for quasars for the two redshift bins. r_0 represents the correlation length, γ represents the power law index, $\log(M_h/M_\odot)$ is the DMH mass. The uncertainty of bias and DMH Mass are calculated from those of r_0 and γ .

4. DISCUSSION

4.1. The Robustness of Clustering Analysis

We present the quasar auto correlation function and the derived halo properties based on a probability threshold of $p_{\text{thre}} = 0.8$. In order to test the robustness and reliability of the clustering analysis, we rerun the entire clustering analysis using the other two probability thresholds of $p_{\text{thre}} = 0.41$ and 0.6 , respectively, from which we obtain the model parameters (r_0 , γ) and infer the bias (b) and DMH mass (M_h), as shown in Table 2.

Remarkably, the measured quasar auto correlation functions for both redshift bins are quite consistent with each other for the different probability thresholds, as shown in Figure 4. The derived clustering model parameters as well as the inferred halo properties are also consistent with each other within the errors, although the model parameters and the derived halo properties using the highest probability threshold for the redshift interval of $5.7 \leq z < 6.3$ show a larger value. For instance, the bias parameters for $5.0 \leq z < 5.7$ for the other two probability thresholds are $b = 12.66^{+0.71}_{-0.72}$ and $b = 13.14^{+0.44}_{-0.44}$, consistent with that using $p_{\text{thre}} = 0.8$, and the derived DMH masses using all probability thresholds are $\sim 10^{12.2} M_\odot$. The excellent agreement leads to two key conclusions: (1) our quasar sample is highly reliable, and the method using probability-weighted pair counting effectively reduces systematic errors from sample contamination; and (2) the clustering methodology and error estimation we have developed are robust.

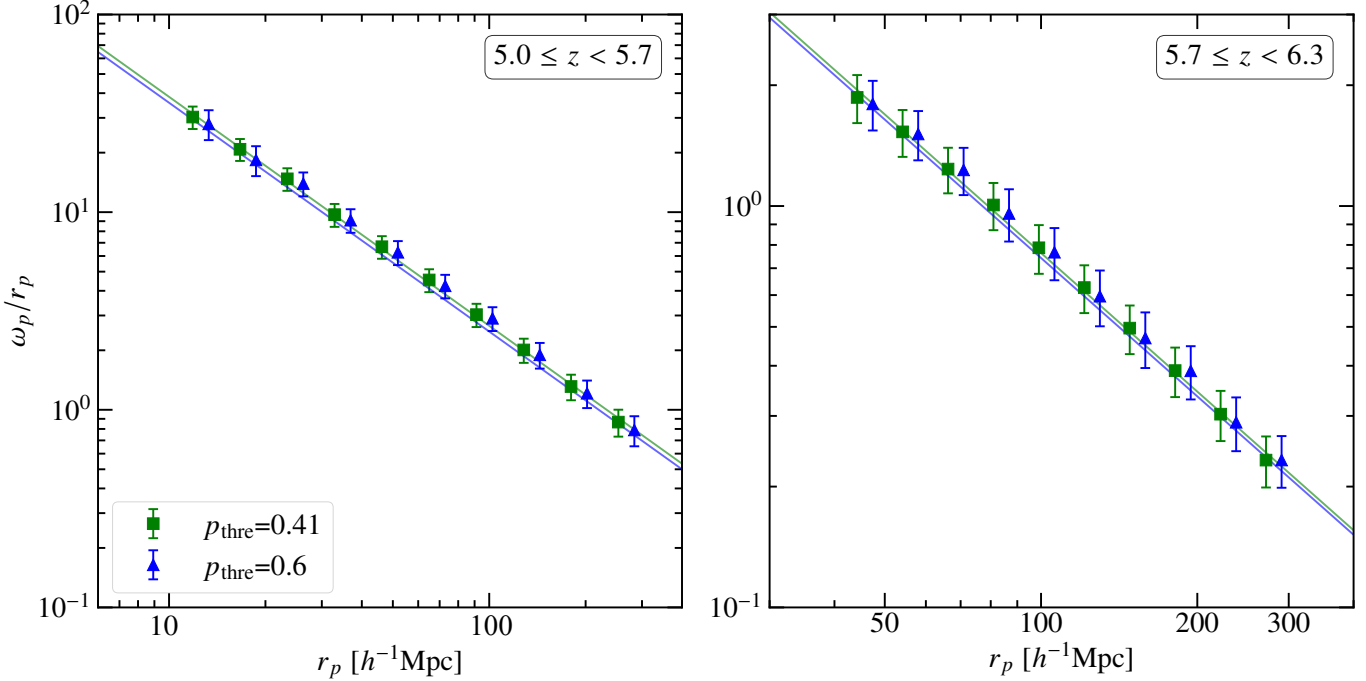


Figure 4. Projected quasar auto correlation function for $5.0 \leq z < 5.7$ (left) and $5.7 \leq z < 6.3$ (right) for $p_{\text{thre}} = 0.41, 0.6$, respectively.

As mentioned in Sec. 2.1, there are two sets of high-redshift quasar candidates selected via the “mag model” or the “flux model” in Ye et al. (2024), both of which are reliable, with the “mag model” having higher precision. All our analysis above is based on the candidates that are simultaneously identified by the “mag model” and the “flux model”. To assess the robustness of our clustering analysis and examine the possible bias introduced by the specific choice of data sample, we perform the same clustering analysis using the high-redshift quasar candidates selected via only the “mag model” or “flux model”. Similarly, we also adopt three probability thresholds of $p_{\text{thre}} = 0.4, 0.6, 0.8$, respectively, to better compare to the results using the “mag model”, and to consider the fact that the probability thresholds of the “flux model” are quite close to those of the “mag model”, see details in Ye et al. (2024).

As expected, the correlation function, as well as the derived halo properties including both the bias parameters and DMH masses using the candidates of the “flux model” or the “mag model” are well consistent with those presented in Table 2 within 1σ error for both $5.0 \leq z < 5.7$ and $5.7 \leq z < 6.3$. That is because, on one hand, the “flux model” is demonstrated to be as robust as the “mag model” (Ye et al. 2024), as verified using DESI DR1 data. On the other hand, the probability-weighted pair counting in constructing the correlation function helps to reduce systematics from sample contamination.

To further test the robustness of clustering analysis and mitigate the sample contamination, we adopt the model success rate to scale the projected correlation function as described in Eq. (1). We multiply DD by 60%, and multiply DR by 60% when constructing the projected correlation function as in Eq. (1), where 60% refers to the model success rate if $p_{\text{thre}} = 0.8$ is imposed to the quasar candidates. The scaled projected correlation function shows good agreement with the results presented in Figure 3, which further demonstrates that the methodology of probability-weighted pair counting in constructing the correlation function helps to reduce systematics from sample contamination.

4.2. DMH Mass Evolution Over Cosmic Time

It is challenging to investigate the cosmic evolution of the dark matter halo mass of the quasars. On one hand, it is not easy to characterize the same quasars across cosmic time, i.e., comparing the quasars with the same luminosity at different cosmic epochs or comparing the quasars with the same luminosity ranking among the entire quasar sample at its corresponding cosmic epoch. On the other hand, the quasar samples from different measurements might be quite different among the quasar intrinsic properties even at the same cosmic epoch.

In Figure 5, we compare the bias parameters and the derived DMH masses with measurements of quasars at different cosmic epochs from the literature (Croom et al. 2005; Shen et al. 2007; Ross et al. 2009; Krumpe et al.

2010; White et al. 2012; Eftekharzadeh et al. 2015; Tmlin et al. 2018; He et al. 2018; Herrero Alonso et al. 2021; Arita et al. 2023; Eilers et al. 2024; Arita et al. 2025; Giner Mascarell et al. 2025; John William et al. 2025; Lin et al. 2025; Ikeda et al. 2025; Schindler et al. 2025a,b) and discuss the possible limitations. Caution that the methods adopted to derive the bias parameters and the DMH masses may vary from one literature to another and the adopted cosmological models might be different among the literature, both of which might lead to a slight differences in the derived bias parameters and DMH masses. Moreover, some studies only provide the minimum halo mass of quasars.

For the bias parameters, we observe an obvious increase of the bias parameters from $z = 0$ to $z \sim 4$ and a flattening for $z > 4$. That is because only more luminous quasars at higher redshift can be observed, and those luminous quasars live in rarer, more massive halos, which are more strongly clustered relative to the dark matter distribution. Qualitatively, our measurements of the bias parameter are close to those at $z > 4$, all of which are ~ 10 . Quantitatively, there exist a large scatter between the different measurements of the bias parameter, which are probably due to the limited data sample at higher redshifts.

For the derived DMH mass estimates, the different measurements suggest that the characteristic dark matter halo mass of quasars does not evolve significantly with redshift up to $z \sim 4$ within the measurement uncertainties. And more measurements at $z > 4$ demonstrate that the low-luminosity quasars or AGNs reside in a less massive dark matter halo, with a typical dark matter halo mass around $10^{11} M_{\odot}$. At $z \sim 5$ –6, our derived DMH masses are slightly higher than the estimation for low-luminosity AGNs, as expected, since our quasar sample are brighter than those low-luminosity AGNs. For example, Arita et al. (2025) reports $\log(M_h/h^{-1} M_{\odot}) = 11.53^{+0.15}_{-0.2}$ for the low-luminosity AGNs, and Lin et al. (2025) also obtains $\log(M_h/M_{\odot}) = 11.06^{+0.36}_{-0.32}$ for the low-luminosity AGNs. However, we also find significant discrepancies between our estimation and the other studies at $z > 6$. Eilers et al. (2024) report a much higher minimum mass of $\log(M_{h,\min}/M_{\odot}) = 12.43^{+0.13}_{-0.15}$ for quasars with typical $M_{1450} \sim -27.5$, and normally the typical halo mass is much higher than the minimum halo mass. And Arita et al. (2023) find $M_h = 5.0^{+7.4}_{-4.0} \times 10^{12} h^{-1} M_{\odot}$ for quasars with much lower typical luminosity of $M_{1450} \sim -24.5$, both of which are higher than our estimate for quasars at $5.7 \leq z < 6.3$. At even higher redshift of $z \sim 7.3$, Schindler et al. (2025b) finds that the minimum dark

matter halo mass of two quasars with $M_{1450} \sim -26.5$ is $11.64^{+0.56}_{-0.64} M_{\odot}$.

Previous studies (Arita et al. 2023; Eilers et al. 2024) suggest a non-evolving dark matter halo mass of quasars, on an order of $10^{12} M_{\odot}$, across cosmic time. However, our results, combined with other measurements of the quasars' DMH masses at $z > 5$ which obtain a much lower DMH mass of $\sim 10^{11.5} M_{\odot}$, suggest a more complex, and possibly non-monotonic evolution of quasar/AGN hosting dark matter halo. Moreover, the minimum dark matter halo mass of quasars shows the trend that it increases as the redshift decreases, as shown in Figure 5, although the uncertainty is comparably large, which further supports the cosmic evolving dark matter halo of quasars.

4.3. Duty Cycle

In the standard model of SMBH growth (Salpeter 1964), SMBH accumulates mass exponentially. The standard scenario assumes that SMBH growth proceeds continuously, resulting in a simple exponential light curve of the SMBH growth. Consequently, these massive SMBHs will appear as luminous quasars for most of their cosmic history. Here we evaluate the duty cycle (f_{duty}) of quasars, which represents the fraction of dark matter halos that host active quasars, to examine the standard model of SMBH growth. It is assumed that a DMH with a minimum mass threshold, $M_{h,\min}$, can host a quasar, thus the duty cycle is defined as the number of observed quasars with minimum luminosity ($M_{1450 \text{ min}}$, short for M_{\min}) to the entire number of host dark matter halos above $M_{h,\min}$, as follows

$$f_{\text{duty}} = \frac{\int_{M_{\min}}^{\infty} \Phi(M) dM}{\int_{M_{h,\min}}^{\infty} n(M_h) dM_h} \quad (12)$$

We adopt $M_{\min} = -24.5$ for $5.0 \leq z < 5.7$ and $M_{\min} = -23$ for $5.7 \leq z < 6.3$. These limits approximately correspond to the observed faint-end magnitudes for each subsample, as shown in Figure 1. $n(M_h)$ represents the DMH mass function at a certain redshift z . $\Phi(M)$ is the quasar luminosity function (QLF) at the same redshift z , which is well approximated by a broken double power-law (i.e., Boyle et al. 2000):

$$\Phi(M, z) = \frac{\Phi^*(z)}{10^{0.4(\alpha+1)(M-M^*)} + 10^{0.4(\beta+1)(M-M^*)}} \quad (13)$$

It is defined by the normalization $\Phi^*(z)$, the break magnitude M^* , and the two power-law slopes α and β . The normalization factor $\Phi^*(z)$ takes the form of the following:

$$\Phi^*(z) = \Phi^*(z = 6) \times 10^{k(z-6)} \quad (14)$$

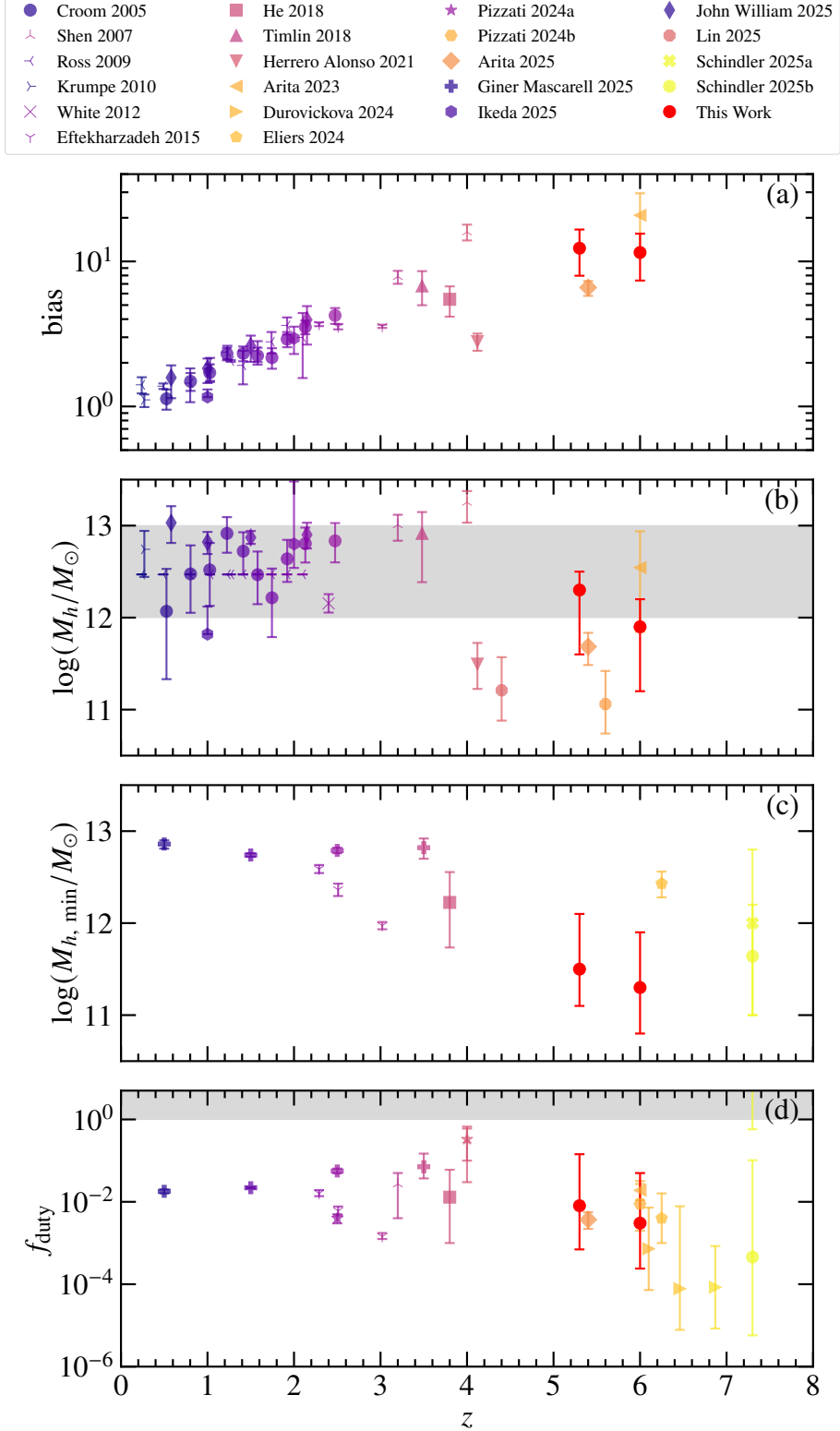


Figure 5. The cosmic evolution of the bias parameters (a), the typical DMH mass (b), the minimum DMH mass (c), the duty cycle (d) based on clustering analysis from $z = 0$ to $z \sim 7.3$. The typical DMH mass estimations are from Croom et al. (2005); Shen et al. (2007); Ross et al. (2009); Krumpe et al. (2010); White et al. (2012); Timlin et al. (2018); Herrero Alonso et al. (2021); Arita et al. (2023, 2025); Ikeda et al. (2025); John William et al. (2025); Lin et al. (2025) and this work, while the minimum DMH masses are from Eftekharzadeh et al. (2015); He et al. (2018); Eilers et al. (2024); Giner Mascarell et al. (2025); Schindler et al. (2025a,b) and this work. Grey shaded area in (b) panel represents the typical DMH mass range of type-I quasars.

where the parameter k describes the exponential evolution of the quasar density with redshift. The typical value of k is -0.47 (Willott et al. 2010) or -0.7 (Jiang et al. 2016). The parameters of the quasar luminosity function are adopted according to Yang et al. (2016) for $4.7 \leq z < 5.4$ and Schindler et al. (2023) for $5.7 \leq z < 6.2$, as shown in Table 3.

z	$\log \Phi^*(z = 6)$	M^*	α	β	k
5.3	$-8.82^{+0.15}_{-0.15}$	$-26.98^{+0.23}_{-0.23}$	-2.03	$-3.58^{+0.24}_{-0.24}$	-0.47
6.0	$-8.75^{+0.47}_{-0.41}$	$-26.38^{+0.79}_{-0.60}$	$-1.70^{+0.29}_{-0.19}$	$-3.84^{+0.63}_{-1.21}$	-0.70

Table 3. The adopted parameters of the QLF for $5.0 \leq z < 5.7$ and $5.7 \leq z < 6.3$.

Here we adopt the DMH mass function proposed by Tinker et al. (2008), as follows

$$\frac{dn}{dM_h} = f(\sigma) \frac{\bar{\rho}_m}{M_h} \frac{d \ln \sigma^{-1}}{dM_h}, \quad (15)$$

$$f(\sigma) = A \left[\left(\frac{\sigma}{b} \right)^{-a} + 1 \right] e^{-c/\sigma^2}. \quad (16)$$

where σ is the same as in Eq. (9). The other parameters are adopted as $A = 0.186$, $a = 1.47$, $b = 2.57$, $c = 1.19$ according to Table 2 in Tinker et al. (2008). It should be noted that this mass function was accomplished using the Python package COLOSSUS⁴ by Diemer (2018). The minimum mass is estimated from the measured bias parameter, which is expressed as

$$b_{\text{eff}} = \frac{\int_{M_{h,\text{min}}}^{\infty} b(M_h, z) n(M_h) dM_h}{\int_{M_{h,\text{min}}}^{\infty} n(M_h) dM_h}, \quad (17)$$

where $b(M, z)$ is the bias parameter of a given DMH at a certain redshift z , which is the same as Eq. (8) and interpreted as the mean bias for DMH whose mass exceed $M_{h,\text{min}}$.

For the quasar sample with $p_{\text{thre}} = 0.8$, we obtain $\log(M_{h,\text{min}}/M_{\odot}) = 11.5^{+0.6}_{-0.4}$ and $\log(f_{\text{duty}}) = -3.79^{+1.22}_{-1.06}$ ($f_{\text{duty}} = 0.00016^{+0.00251}_{-0.00015}$) for $5.0 \leq z < 5.7$, and $\log(M_{h,\text{min}}/M_{\odot}) = 11.3^{+0.6}_{-0.5}$ and $\log(f_{\text{duty}}) = -4.18^{+1.26}_{-1.12}$ ($f_{\text{duty}} = 0.00007^{+0.00115}_{-0.00006}$) for $5.7 \leq z < 6.3$. The comparison between our measurements of the quasar duty cycle and the literature values is presented in Figure 5. The new measurements of QLF for $5.7 \leq z < 6.3$ (Ye, Zhang et al. 2026) show good agreements with the TRINITY model (Zhang et al. 2023, 2024), both of which are approximately one order of

magnitude higher than the QLF measurements at $z \sim 6$ in Schindler et al. (2023). Although there is no direction measurement of the QLF for $5.0 \leq z < 5.7$ ($z \sim 5.3$) in Ye, Zhang et al. (2026), the TRINITY prediction of the QLF for $z \sim 5.3$ is also approximately one order of magnitude higher than the QLF measurement at $z \sim 5.3$ in Yang et al. (2016). TRINITY is a flexible empirical model that self-consistently infers the statistical connection between dark matter haloes, galaxies, and supermassive black holes from $z = 10$ to $z = 0$ uniquely, robustly, and self-consistently. A comprehensive picture of galaxy – SMBH coevolution is synthesized from multiple observational probes in the TRINITY model. These include the QLF, the active black hole mass function (ABHMF), the local bulge – black hole mass scaling relation, and critically the quasar probability distribution function (QPDF). The QPDF is a vital diagnostic, as it directly constrains AGN duty cycles and reveals the divergent growth histories across different halo, galaxy, and SMBH populations. If we adopt those new measurements, the f_{duty} becomes over one order of magnitude larger: $f_{\text{duty}} = 0.008^{+0.135}_{-0.007}$ for $5.0 \leq z < 5.7$, and $f_{\text{duty}} = 0.003^{+0.047}_{-0.003}$ for $5.7 \leq z < 6.3$. These results are consistent with $0.0037^{+0.0019}_{-0.0015}$ at $z \sim 5.5$ (Arita et al. 2025) and 0.019 ± 0.008 at $z \sim 6$ (Arita et al. 2023).

5. SUMMARY

In this paper, we perform the clustering analysis of high-redshift quasar candidates at $5.0 \leq z < 6.3$, selected from the combined data of LS DR9 and WISE via machine learning technique. The typical M_{1450} of those quasar candidates is ~ -25.5 for $5.0 \leq z < 5.7$ and -25 at $5.7 \leq z < 6.3$. The quasar candidates sample are demonstrated to be quite reliable using DESI DR1 spectra, with a success rate of $\gtrsim 60\%$ if we impose a probability threshold of 0.8. Our main conclusions are summarized as follows:

1. We estimate the quasar projected auto correlation function for $5.0 \leq z < 5.7$ and $5.7 \leq z < 6.3$. The results are well fit by the real-space correlation function expressed by a power-law function $\xi(r) = (r/r_0)^{-\gamma}$, implying a strong clustering of quasars at large scale. From the the best-fit to the projected auto correlation function, we obtain $r_0 = 20.76 \pm 6.18 \text{ h}^{-1}\text{Mpc}$, and a slightly shallower power-law index of $\gamma = 1.17 \pm 0.05$ for $5.0 \leq z < 5.7$, from which the DMH mass is evaluated as $\log(M_h/M_{\odot}) = 12.2^{+0.2}_{-0.7}$ with the bias parameter, $b = 12.34^{+4.26}_{-4.37}$ for $p_{\text{thre}} = 0.8$. And the DMH mass is estimated to be $\log(M_h/M_{\odot}) = 11.9^{+0.3}_{-0.7}$ with the bias parameter, $b = 11.52^{+4.02}_{-4.14}$ for quasars at $5.7 \leq z < 6.3$ for $p_{\text{thre}} = 0.8$.

⁴ <https://bitbucket.org/bdiemer/colossus/src/master/>

2. We find that the projected auto correlation function, as well as the derived halo properties (M_h and b) is not sensitive to the probability thresholds we choose, which demonstrates the reliability of the data sample and the robustness of the clustering methodology by weighting the pair counting with the predicted probability in the construction of the projected auto correlation function.
3. Although the comparison across the different measurements of quasars' hosting dark matter halos might introduce systematic uncertainties, the broad trend across cosmic time offers insight into the evolution of quasars' dark matter halo. The bias parameter shows a clear increase from $z \sim 0$ to $z \sim 4$, then appears to plateau at $z > 4$. The characteristic halo mass, in contrast, shows little evolution up to $z \sim 4$. At higher redshifts ($z > 4$), however, multiple studies suggest a lower characteristic halo mass compared to the $z < 4$ population. Together, these trends indicate a complex, potentially non-monotonic evolution of quasar host dark matter halos across cosmic time.
4. We estimate the quasar duty cycle f_{duty} for both redshift intervals of $5.0 \leq z < 5.7$ and $5.7 \leq z < 6.3$ by adopting the current QLF measurements and a dark matter halo mass function, with a value of $\log(f_{\text{duty}}) = 3.79_{-1.06}^{+1.22}$ for $5.0 \leq z < 5.7$ and $\log(f_{\text{duty}}) = -4.18_{-1.12}^{+1.26}$ for $5.7 \leq z < 6.3$. The duty cycle becomes $0.008_{-0.007}^{+0.135}$ for $5.0 \leq z < 5.7$ and $0.003_{-0.003}^{+0.047}$ for $5.7 \leq z < 6.3$ if we adopt a new measurement of QLF or the theoretical predictions of the QLF from the TRINITY model.

6. ACKNOWLEDGMENTS

HM, HZ and GY acknowledge financial support from the start-up funding of the Huazhong University of Sci-

ence and Technology, the National Science Foundation of China grant (No. 12303007) and the China Manned Space Program (CMS-CSST-2025-A06).

This research used data obtained with the Dark Energy Spectroscopic Instrument (DESI). DESI construction and operations are managed by the Lawrence Berkeley National Laboratory. This material is based upon work supported by the U.S. Department of Energy, Office of Science, Office of High-Energy Physics, under Contract No. DE-AC02-05CH11231, and by the National Energy Research Scientific Computing Center, a DOE Office of Science User Facility under the same contract. Additional support for DESI was provided by the U.S. National Science Foundation (NSF), Division of Astronomical Sciences under Contract No. AST-0950945 to the NSF's National Optical-Infrared Astronomy Research Laboratory; the Science and Technology Facilities Council of the United Kingdom; the Gordon and Betty Moore Foundation; the Heising-Simons Foundation; the French Alternative Energies and Atomic Energy Commission (CEA); the National Council of Science and Technology of Mexico (CONACYT); the Ministry of Science and Innovation of Spain (MICINN), and by the DESI Member Institutions: www.desi.lbl.gov/collaborating-institutions. The DESI collaboration is honored to be permitted to conduct scientific research on Iolkam Du'ag (Kitt Peak), a mountain with particular significance to the Tohono O'odham Nation. Any opinions, findings, and conclusions or recommendations expressed in this material are those of the author(s) and do not necessarily reflect the views of the U.S. National Science Foundation, the U.S. Department of Energy, or any of the listed funding agencies.

Based on observations collected at the European Southern Observatory under ESO programme(s) 109.238W.003, 105.208F.001, and 0104.A-0812(A), and/or data obtained from the ESO Science Archive Facility with DOI(s) under <https://doi.org/10.18727/archive/41>.

REFERENCES

Arita, J., Kashikawa, N., Onoue, M., et al. 2025, MNRAS, 536, 3677, doi: [10.1093/mnras/stae2765](https://doi.org/10.1093/mnras/stae2765)

Arita, J., Kashikawa, N., Matsuoka, Y., et al. 2023, ApJ, 954, 210, doi: [10.3847/1538-4357/ace43a](https://doi.org/10.3847/1538-4357/ace43a)

Bañados, E., Venemans, B. P., Mazzucchelli, C., et al. 2018, Nature, 553, 473, doi: [10.1038/nature25180](https://doi.org/10.1038/nature25180)

Begelman, M. C., Volonteri, M., & Rees, M. J. 2006, MNRAS, 370, 289, doi: [10.1111/j.1365-2966.2006.10467.x](https://doi.org/10.1111/j.1365-2966.2006.10467.x)

Boyle, B. J., Shanks, T., Croom, S. M., et al. 2000, MNRAS, 317, 1014, doi: [10.1046/j.1365-8711.2000.03730.x](https://doi.org/10.1046/j.1365-8711.2000.03730.x)

Carroll, S. 2000, Living Reviews in Relativity, 4, doi: [10.12942/lrr-2001-1](https://doi.org/10.12942/lrr-2001-1)

Cole, S., & Kaiser, N. 1989, MNRAS, 237, 1127, doi: [10.1093/mnras/237.4.1127](https://doi.org/10.1093/mnras/237.4.1127)

Croom, S. M., Smith, R. J., Boyle, B. J., et al. 2001, MNRAS, 322, L29, doi: [10.1046/j.1365-8711.2001.04474.x](https://doi.org/10.1046/j.1365-8711.2001.04474.x)

Croom, S. M., Boyle, B. J., Shanks, T., et al. 2005, *Monthly Notices of the Royal Astronomical Society*, 356, 415, doi: [10.1111/j.1365-2966.2004.08379.x](https://doi.org/10.1111/j.1365-2966.2004.08379.x)

Davis, M., & Peebles, P. J. E. 1983, *ApJ*, 267, 465, doi: [10.1086/160884](https://doi.org/10.1086/160884)

DESI Collaboration, Abdul-Karim, M., Adame, A. G., et al. 2025, arXiv e-prints, arXiv:2503.14745, doi: [10.48550/arXiv.2503.14745](https://doi.org/10.48550/arXiv.2503.14745)

Dey, A., Schlegel, D. J., Lang, D., et al. 2019, *AJ*, 157, 168, doi: [10.3847/1538-3881/ab089d](https://doi.org/10.3847/1538-3881/ab089d)

Di Matteo, T., Springel, V., & Hernquist, L. 2005, *Nature*, 433, 604, doi: [10.1038/nature03335](https://doi.org/10.1038/nature03335)

Diemer, B. 2018, *ApJS*, 239, 35, doi: [10.3847/1538-4365/aaee8c](https://doi.org/10.3847/1538-4365/aaee8c)

Drake, A. B., Farina, E. P., Neeleman, M., et al. 2019, *ApJ*, 881, 131, doi: [10.3847/1538-4357/ab2984](https://doi.org/10.3847/1538-4357/ab2984)

Driver, S. P., & Robotham, A. S. G. 2010, *MNRAS*, 407, 2131, doi: [10.1111/j.1365-2966.2010.17028.x](https://doi.org/10.1111/j.1365-2966.2010.17028.x)

Efstathiou, G., & Rees, M. J. 1988, *MNRAS*, 230, 5p, doi: [10.1093/mnras/230.1.5P](https://doi.org/10.1093/mnras/230.1.5P)

Eltekhzadeh, S., Myers, A. D., White, M., et al. 2015, *Monthly Notices of the Royal Astronomical Society*, 453, 2779, doi: [10.1093/mnras/stv1763](https://doi.org/10.1093/mnras/stv1763)

Eilers, A.-C., Mackenzie, R., Pizzati, E., et al. 2024, *ApJ*, 974, 275, doi: [10.3847/1538-4357/ad778b](https://doi.org/10.3847/1538-4357/ad778b)

Fan, X., Strauss, M. A., Becker, R. H., et al. 2006, *AJ*, 132, 117, doi: [10.1086/504836](https://doi.org/10.1086/504836)

Gardner, J. P., Mather, J. C., Abbott, R., et al. 2023, *PASP*, 135, 068001, doi: [10.1088/1538-3873/acd1b5](https://doi.org/10.1088/1538-3873/acd1b5)

Giner Mascarell, M., Eilers, A.-C., & Storey-Fisher, K. 2025, arXiv e-prints, arXiv:2511.17413, doi: [10.48550/arXiv.2511.17413](https://doi.org/10.48550/arXiv.2511.17413)

Haiman, Z., & Hui, L. 2001, *ApJ*, 547, 27, doi: [10.1086/318330](https://doi.org/10.1086/318330)

He, W., Akiyama, M., Bosch, J., et al. 2018, *PASJ*, 70, S33, doi: [10.1093/pasj/psx129](https://doi.org/10.1093/pasj/psx129)

Herrero Alonso, Y., Krumpe, M., Wisotzki, L., et al. 2021, *A&A*, 653, A136, doi: [10.1051/0004-6361/202141226](https://doi.org/10.1051/0004-6361/202141226)

Ikeda, H., Miyaji, T., Oogi, T., et al. 2025, *ApJ*, 982, 192, doi: [10.3847/1538-4357/adb719](https://doi.org/10.3847/1538-4357/adb719)

Inayoshi, K., Visbal, E., & Haiman, Z. 2020, *ARA&A*, 58, 27, doi: [10.1146/annurev-astro-120419-014455](https://doi.org/10.1146/annurev-astro-120419-014455)

Jiang, L., McGreer, I. D., Fan, X., et al. 2016, *ApJ*, 833, 222, doi: [10.3847/1538-4357/833/2/222](https://doi.org/10.3847/1538-4357/833/2/222)

John William, A., Bilicki, M., Hellwing, W. A., Nakoneczny, S. J., & Jalan, P. 2025, arXiv e-prints, arXiv:2511.17311, doi: [10.48550/arXiv.2511.17311](https://doi.org/10.48550/arXiv.2511.17311)

Kormendy, J., & Richstone, D. 1995, *ARA&A*, 33, 581, doi: [10.1146/annurev.aa.33.090195.003053](https://doi.org/10.1146/annurev.aa.33.090195.003053)

Krumpe, M., Miyaji, T., & Coil, A. L. 2010, *ApJ*, 713, 558, doi: [10.1088/0004-637X/713/1/558](https://doi.org/10.1088/0004-637X/713/1/558)

Landy, S. D., & Szalay, A. S. 1993, *ApJ*, 412, 64, doi: [10.1086/172900](https://doi.org/10.1086/172900)

Lin, X., Fan, X., Sun, F., et al. 2025, arXiv e-prints, arXiv:2505.02896, doi: [10.48550/arXiv.2505.02896](https://doi.org/10.48550/arXiv.2505.02896)

Liu, W., Fan, X., Li, H., et al. 2025, arXiv e-prints, arXiv:2509.08793, doi: [10.48550/arXiv.2509.08793](https://doi.org/10.48550/arXiv.2509.08793)

Lynden-Bell, D. 1969, *Nature*, 223, 690, doi: [10.1038/223690a0](https://doi.org/10.1038/223690a0)

Mainzer, A., Bauer, J., Grav, T., et al. 2011, *ApJ*, 731, 53, doi: [10.1088/0004-637X/731/1/53](https://doi.org/10.1088/0004-637X/731/1/53)

Martini, P., & Weinberg, D. H. 2001, *ApJ*, 547, 12, doi: [10.1086/318331](https://doi.org/10.1086/318331)

Murray, S., Diemer, B., Chen, Z., et al. 2021, *Astronomy and Computing*, 36, 100487, doi: <https://doi.org/10.1016/j.ascom.2021.100487>

Murray, S., Power, C., & Robotham, A. 2013, *Astronomy and Computing*, 3-4, 23, doi: <https://doi.org/10.1016/j.ascom.2013.11.001>

Overzier, R. A., Guo, Q., Kauffmann, G., et al. 2009, *MNRAS*, 394, 577, doi: [10.1111/j.1365-2966.2008.14264.x](https://doi.org/10.1111/j.1365-2966.2008.14264.x)

Peebles, P. J. E. 1980, *The large-scale structure of the universe* (Princeton University Press)

Planck Collaboration, Aghanim, N., Akrami, Y., et al. 2020, *A&A*, 641, A1, doi: [10.1051/0004-6361/201833880](https://doi.org/10.1051/0004-6361/201833880)

Regan, J. A., Johansson, P. H., & Haehnelt, M. G. 2014, *MNRAS*, 439, 1160, doi: [10.1093/mnras/stu068](https://doi.org/10.1093/mnras/stu068)

Robertson, B. E. 2010, *ApJL*, 716, L229, doi: [10.1088/2041-8205/716/2/L229](https://doi.org/10.1088/2041-8205/716/2/L229)

Ross, N. P., Shen, Y., Strauss, M. A., et al. 2009, *The Astrophysical Journal*, 697, 1634–1655, doi: [10.1088/0004-637x/697/2/1634](https://doi.org/10.1088/0004-637x/697/2/1634)

Salpeter, E. 1964, *Astrophysical Journal*, vol. 140, p. 796–800, 140, 796

Salpeter, E. E. 1964, *ApJ*, 140, 796, doi: [10.1086/147973](https://doi.org/10.1086/147973)

Schindler, J.-T., Bañados, E., Connor, T., et al. 2023, *ApJ*, 943, 67, doi: [10.3847/1538-4357/aca7ca](https://doi.org/10.3847/1538-4357/aca7ca)

Schindler, J.-T., Hennawi, J. F., Davies, F. B., et al. 2025a, *Nature Astronomy*, doi: [10.1038/s41550-025-02660-1](https://doi.org/10.1038/s41550-025-02660-1)

—. 2025b, arXiv e-prints, arXiv:2510.08455, doi: [10.48550/arXiv.2510.08455](https://doi.org/10.48550/arXiv.2510.08455)

Schlegel, D., Dey, A., Herrera, D., et al. 2021, in *American Astronomical Society Meeting Abstracts*, Vol. 237, *American Astronomical Society Meeting Abstracts #237*, 235.03

Shanks, T., & Boyle, B. J. 1994, *MNRAS*, 271, 753, doi: [10.1093/mnras/271.4.753](https://doi.org/10.1093/mnras/271.4.753)

Shen, Y., Strauss, M. A., Oguri, M., et al. 2007, *The Astronomical Journal*, 133, 2222, doi: [10.1086/513517](https://doi.org/10.1086/513517)

Shen, Y., McBride, C. K., White, M., et al. 2013, *ApJ*, 778, 98, doi: [10.1088/0004-637X/778/2/98](https://doi.org/10.1088/0004-637X/778/2/98)

Sheth, R. K., & Tormen, G. 1999, *Monthly Notices of the Royal Astronomical Society*, 308, 119, doi: [10.1046/j.1365-8711.1999.02692.x](https://doi.org/10.1046/j.1365-8711.1999.02692.x)

Sinha, M., & Garrison, L. H. 2020, *MNRAS*, 491, 3022, doi: [10.1093/mnras/stz3157](https://doi.org/10.1093/mnras/stz3157)

Timlin, J. D., Ross, N. P., Richards, G. T., et al. 2018, *The Astrophysical Journal*, 859, 20, doi: [10.3847/1538-4357/aab9ac](https://doi.org/10.3847/1538-4357/aab9ac)

Tinker, J., Kravtsov, A. V., Klypin, A., et al. 2008, *ApJ*, 688, 709, doi: [10.1086/591439](https://doi.org/10.1086/591439)

Tinker, J. L., Robertson, B. E., Kravtsov, A. V., et al. 2010, *The Astrophysical Journal*, 724, 878, doi: [10.1088/0004-637X/724/2/878](https://doi.org/10.1088/0004-637X/724/2/878)

Ucci, G., Dayal, P., Hutter, A., et al. 2021, *MNRAS*, 506, 202, doi: [10.1093/mnras/stab1229](https://doi.org/10.1093/mnras/stab1229)

Volonteri, M. 2012, *Science*, 337, 544, doi: [10.1126/science.1220843](https://doi.org/10.1126/science.1220843)

Wang, F., Yang, J., Fan, X., et al. 2021, *ApJL*, 907, L1, doi: [10.3847/2041-8213/abd8c6](https://doi.org/10.3847/2041-8213/abd8c6)

White, M., Myers, A. D., Ross, N. P., et al. 2012, *MNRAS*, 424, 933, doi: [10.1111/j.1365-2966.2012.21251.x](https://doi.org/10.1111/j.1365-2966.2012.21251.x)

Willott, C. J., Delorme, P., Reylé, C., et al. 2010, *AJ*, 139, 906, doi: [10.1088/0004-6256/139/3/906](https://doi.org/10.1088/0004-6256/139/3/906)

Wright, E. L., Eisenhardt, P. R. M., Mainzer, A. K., et al. 2010, *AJ*, 140, 1868, doi: [10.1088/0004-6256/140/6/1868](https://doi.org/10.1088/0004-6256/140/6/1868)

Yang, J., Wang, F., Wu, X.-B., et al. 2016, *ApJ*, 829, 33, doi: [10.3847/0004-637X/829/1/33](https://doi.org/10.3847/0004-637X/829/1/33)

Yang, J., Wang, F., Fan, X., et al. 2020, *ApJL*, 897, L14, doi: [10.3847/2041-8213/ab9c26](https://doi.org/10.3847/2041-8213/ab9c26)

Ye, G., Zhang, H., & Wu, Q. 2024, *ApJS*, 275, 19, doi: [10.3847/1538-4365/ad79ee](https://doi.org/10.3847/1538-4365/ad79ee)

Zehavi, I., Zheng, Z., Weinberg, D. H., et al. 2005, *The Astrophysical Journal*, 630, 1, doi: [10.1086/431891](https://doi.org/10.1086/431891)

Zhang, H., Behroozi, P., Volonteri, M., et al. 2024, *MNRAS*, 529, 2777, doi: [10.1093/mnras/stae655](https://doi.org/10.1093/mnras/stae655)

—. 2023, *MNRAS*, 518, 2123, doi: [10.1093/mnras/stac2633](https://doi.org/10.1093/mnras/stac2633)

Zhang, H., Ye, G., Wu, R., & Zaritsky, D. 2025, *ApJS*, 278, 18, doi: [10.3847/1538-4365/adbfoa](https://doi.org/10.3847/1538-4365/adbfoa)